In-process defect monitoring and correction in additive manufacturing of aluminum alloys

Behrooz Jalalahmadi
Sentient Science
Buffalo, NY, USA

Jingfu Liu
Sentient Science
Buffalo, NY, USA

Jason Rios
Sentient Science
Buffalo, NY, USA

John Slotwinski
Johns Hopkins University
Applied Physics Laboratory
Laurel, MD, USA

Christopher Peitsch
Johns Hopkins University
Applied Physics Laboratory
Laurel, MD, USA

Arnold Goldberg
Johns Hopkins University
Applied Physics Laboratory
Laurel, MD, USA

Timothy Montalbano
Johns Hopkins University
Applied Physics Laboratory
Laurel, MD, USA

ABSTRACT

Metal additive manufacturing (AM) has become increasingly popular to fabricate complex, light-weight, and high-efficiency components for use in the aerospace industry; however, there are inherent limitations in existing AM processes that have delayed widespread implementation for aviation applications. Porosity is just one example of the key characteristics that can impact the mechanical strength of an AM part. This research focuses on a real-time feedback system to detect and correct defects during the powder bed fusion process of aluminum alloys. In this study, AlSi10Mg coupons were built using various AM parameters. The build process was continuously monitored via a high-frequency in-situ infrared camera which had been integrated into a commercial metal powder bed fusion machine. Porosity information (pore location and size) of the as-built AM coupons were characterized using x-ray computed tomography. The monitoring results were post processed and correlated with porosity location, indicating a strong relationship between abnormal sensing signal and pore formation. This demonstrates that the real-time abnormal sensing signal can be a good indicator for identifying pore formation during the AM process. Additionally, Sentient Science Corporation (Sentient) used its advanced modeling technique to simulate the AM build process regarding the melt pool geometry, porosity, and microstructure. Prediction of porosity level at different AM parameters aligned well with the experimental results. Advanced modeling results showed that careful selection of AM settings is required to correct in-process defects. Repair parameters must be tailored to achieve satisfactory correction of individual defects. Combining the in-situ defect monitoring and advanced simulation capabilities enables the creation of a closed-loop feedback control system that provides automatic defect detection and correction action in powder bed additive manufacturing process.

INTRODUCTION

Army rotorcraft components require structural integrity to be flight safe. Traditional manufacturing methods have been refined over time to achieve high reliability such as casting processes used for gearbox housings or machining used for mounts, fittings, and pitch-link horns. Recent progress with use of additive manufacturing (AM), especially powder bed fusion processes, has demonstrated strong capability to manufacture complex components as a single part, which may save manufacturing labor, cost, and reduce production time. In addition, the application of optimized topology in design of AM parts can have the added benefit of weight savings unfeasible using traditional manufacturing processes. However, there are inherent limitations in existing AM processes that have delayed widespread implementation for aviation applications.

Among those limitations, process-induced defects are one of the main concerns for current metal AM technology. Various types of defects would be expected in AM processes, such as porosity, un-melted particles, grain anisotropy, balling effects, material inhomogeneity, residual stress, and distortion [1]. The relationship between AM process parameters and part quality have been studied and reported extensively [2]. A high-energy density in AM process will cause the balling effect that results in high surface roughness and

---

Presented at the Vertical Flight Society's 75th Annual Forum & Technology Display, Philadelphia, PA, USA, May 13-16, 2019.

microstructural in-homogeneities, while a low-energy density usually causes material discontinuities, such as porosity and delamination of adjunctive passes/layers. Appropriate process parameters are essential to build defect-free parts, and most commercial metal AM machines have built-in parameter settings which are supposed to print defect-free parts. However, in an actual printing process, inherent variability of AM processes (e.g. random distribution of AM powder, melt pool flow, denudation process) usually cause deviation from ideal experimental conditions, resulting in process defects. To improve process stability, in-process monitoring is a well-known approach to monitor the process variation, and then make timely correction to eliminate process defects.

Several works in literature have reported the studies of monitoring AM processes. Different sensors, such as thermocouple, pyrometer, thermal camera, high-speed camera and so on, have been attempted to monitor abnormal signals from AM processes which would help identify any potential defect. Details of those works can be found in the review literature [2-4]. Most current sensors are used to monitor the melt pool geometry, but they are not able to monitor the defects, such as pores. Also, those sensors are not fast enough to capture the printing details at micro time scale, and they may also have degraded monitoring accuracy when operating with complex AM processes (e.g. disturbance from metallic debris, rapid transition of material states). Recently, John Hopkins University Applied Physics Laboratory (JHU/APL) reported research on monitoring the relative temperature change during the build using a high-frequency infrared (IR) camera. This approach was able to detect in real time unwanted process deviations. It measured unexpected differences in process temperature that is possibly indicative of an undesirable process change [5]. Lawrence Livermore National Lab (LLNL) has recently reported a study of machine-learning-based monitoring of laser powder bed fusion process [6]. Sets of melt pool data were acquired using visual imaging equipment, and then a machine-learning-based model was developed, trained with those data, and evaluated for capability to predict melt pool track widths. This machine-learning-based monitoring was demonstrated to enable on-the-fly assessment of laser track welds. This research provides a new idea to potentially identify process defects in real time.

As discussed above, most relevant works are limited to monitor the AM process, and sensing data were usually *ex-situ* examined. In this circumstance, process-induced defects may be identified by post analyzing sensing data, but correcting those defects using post build processes (e.g. hot isostatic pressure, heat treatment), if possible, would be time and/or cost prohibitive. This study aims to advance current technique by building a close-loop feedback control system that enables monitoring and defect correction in real time for powder bed fusion of aluminum alloys. In order to achieve this goal, several key issues need to be addressed: 1) how to accurately identify defects at each printed layer; 2) how to choose optimal process parameters to correct specific defects; 3) how to manage / process enormous data in real time, including processing *in-situ* monitoring signals in real time, dynamically determining optimal repair parameter sets in real time; and 4) integrating relevant hardware and software in AM machine's control system.

In this paper, efforts of *in-situ* monitoring process defects and optimizing process parameters through advanced simulation will be presented. Relevant experimental validation will be presented to demonstrate the technical feasibility of a close-loop feedback AM system for monitoring and correcting process defects. Plans for developing a prototype machine will be also discussed. The paper will be outlined as following sections: 1) *in-situ* monitoring of laser powder bed fusion process in printing aluminum coupons; 2) material characterization to examine process-induced defects; 3) data analysis to correlate sensing signals with process-induced defects; 4) advanced AM process modeling and validation; 5) constructing a process window for optimal defect-repair parameters; and 6) follow-on work

IN-SITU MONITORING OF LASER POWDER BED FUSION PROCESS USING INFRARED CAMERA

Total of 15 AlSi10Mg cube coupons were built with various parameters using a laser powder bed fusion process machine (EOS M290 shown in Fig. 1). The entire printing process was monitored using a high-frequency long wavelength infrared (IR) camera that was integrated in the EOS M290 machine. Experiments were performed at JHU/APL. Details of the experimental set-up and relevant results are described below:

Fig.1 EOS M290 laser powder bed fusion system at JHU/APL.

Thermal sensor selection and set-up

There have been a variety of implementations of in-situ sensors for metal AM processes [2]. True-temperature measurements using thermal cameras have received significant attention. However, these systems are very expensive, difficult to calibrate properly, difficult to integrate into metal AM systems, and can only see a small area of the build. Here, our approach is to use relative-temperature thermal cameras. The relative temperature approach will not be useful for computational model validation, but it could measure unexpected differences in process temperature that may be indicative of an undesirable process change.

The infrared (IR) camera used to view the AM process was integrated by JHU/APL from commercially-available components. At the heart of the camera was a “sensor engine” based on a quantum well infrared photodetector (QWIP) focal plane array (FPA) in an integrated dewar/cooler assembly (IDCA) which uses a Stirling cycle mechanical cooler to cool the FPA to 65 K. This camera is sensitive in the long wavelength infrared (LWIR, wavelengths between 8 µm and 12 µm) spectrum. This spectral range was chosen because of the inherently low thermal contrast for blackbody emission in this band. That is, the rate of change of emitted power from an object for a change in its temperature is low compared to other regions of the spectrum. Unlike the detectors in the LWIR microbolometer cameras that have come into widespread use, the detectors in this FPA are photon detectors and therefore are able to capture very fast phenomenology (detector time constant < 1 ns). By contrast, microbolometer cameras are thermal sensors with time constants on the order of 10 ms. The full frame format of the FPA was 640×512 pixels but the camera was set up to only run the central 128×128 region of the array in order to enable a high frame rate (1.313 kHz) to be achieved and the integration time used for the experiment was 49 µs. The top of the AM chamber has a port that is normally blanked off but for this experiment the anodized aluminum blank was replaced by a zinc selenide (ZnSe) window which was specified to have at least 70% transmission in the pass-band of the camera. The setup is shown in Fig. 2.

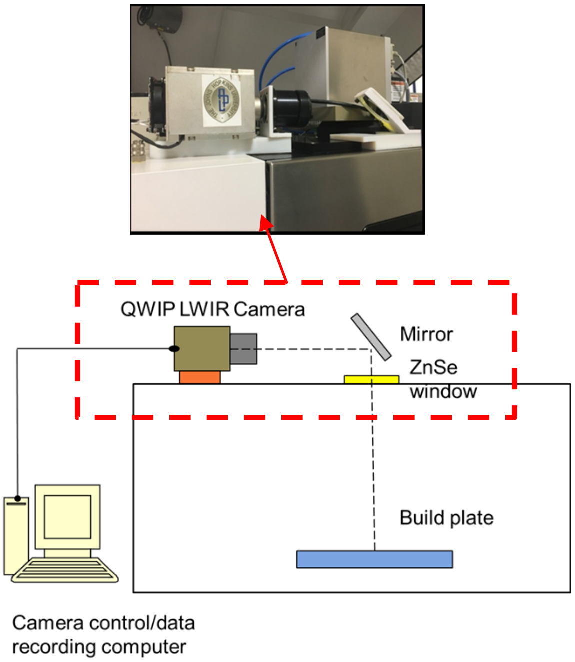

Fig.2 In-situ IR camera set-up.

AM process parameters and coupon geometry

A total of 15 AlSi10Mg coupons were built using various AM parameters. The building process was continuously monitored via a high-frequency in-situ infrared camera which had been integrated into a commercial metal powder system. Each coupon has the dimension of 5mm × 5 mm × 10 mm. Table 1 lists the 5 different process parameters in this study. Each parameter was repeated 3 times (“A1” represents parameter A 1st repeat). Sample #C were built using vendor-provided receipt and used as the benchmark. Its nominal energy density was 100%. Other samples (A, B, D, E) were built using modified nominal energy density in order to create “artificial” defects. Laser power and scan speed were varied to achieve different energy density.

Table 1. AM process parameters.

Sample #	Energy Density (J/mm^3)	Nominal Energy density
A	12.48	25%
B	24.97	50%
C	49.93	100%
D	74.87	150%
E	99.87	200%

[a] Specific parameter is not included due to vendor intellectual property

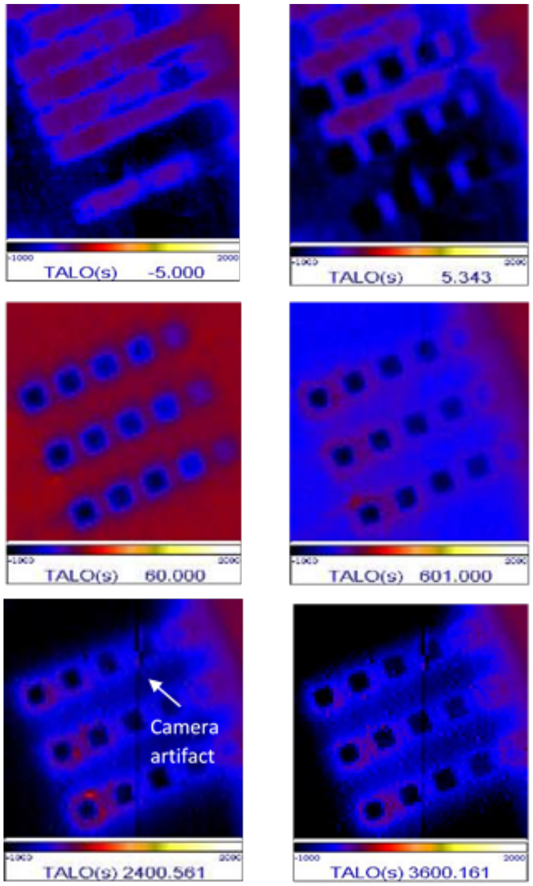

Fig.3 Examples of IR images at different times. Color intensity represents radiance value. (“TALO” = Time since first indication of laser)

Collect IR camera data

The entire build process has been recorded using the IR camera through the build of 76 min 9 sec (4569 s) at a frame rate of 1300 Hz. 25 mm focal length f/2.3 lens gave a pixel size at the target of 0.76 mm (~6.5 pixels across each part). The IR camera was calibrated using a cavity blackbody source. There is a total over 6 million frames of images, resulting in ~30GB of data. Fig. 3 shows some examples of thermal images at different time steps. TALO in the figure means the time since first indication of laser. The vertical line seen in the imagery after about T+1200 s is due to an artifact in the camera itself that could not be fully corrected out. The area of artifacts will not be considered in the following analysis.

MATERIAL CHARACTERIZATION

Material characterization of AlSi10Mg coupons were focused on porosity examination, since porosity is the type of defect that causes the most concern. Two analytic methods, namely optical microcopy analysis and x-ray computed tomography (XRCT) analysis were used to examine all coupons built using the 5 AM conditions. Details will be discussed below:

Optical microscopy analysis

AlSi10Mg coupons were mounted in epoxy after the AM build process. Coupons were ground using SiC papers down to 1200 grit, and then polished using diamond suspension which started at 9 µm and finished at 0.5 µm. Final polishing was performed using 0.02 µm colloidal silica. The orientation of each coupon during grinding is shown in Fig. 4.

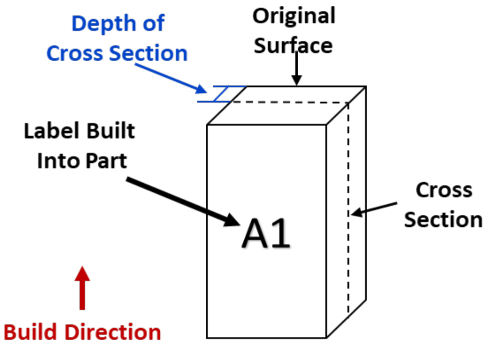

Fig.4 Coupon preparation for optical microscopy characterization.

Fig. 5 shows the optical microscopy of the cross section of 5 coupons processed using increasing laser energy density. Porosity can be seen in all coupons. A1 has the largest degree of irregular shaped pores due to lack of fusion at low laser energy density. Porosity is minimized in C1 which was processed at near optimal laser energy density. D1 and E1 have increasing amounts of spherical pores compared to A1/B1 samples. Those spherical voids were likely generated under keyhole phenomenon which formed at high laser energy density. From Fig. 5, we can clearly tell the difference of void size and geometry at different AM conditions. Lack-of-fusion voids are irregular in shape, and have much lower sphericity than keyhole voids. It should be noted that the top region of all coupons look defect-free, because the last three built-layers use the vendor's default parameter (#C) which is different from the designated condition. This is from the AM machine default configuration, and applies to all other samples (B-E).

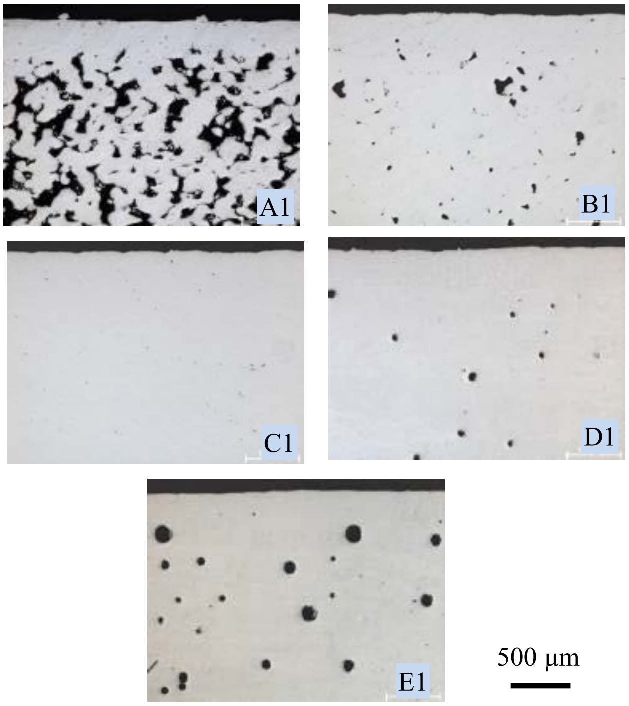

Fig. 5 Cross section of 5 coupons processed using increasing laser energy density

X-ray Computed Tomography (XRCT) analysis

XRCT was performed on 10 coupons (A2, A3, B2, B3, C2, C3, D2, D3, E2, E3) to identify the presence of porosity as well as individual pore location, size, and geometry. The scans were performed on a North Star Imaging (NSI) X050 system and the volume data reconstructed using NSI efX-CT software. The resulting voxel resolution is 7.7 microns. Fig. 6 shows the XRCT coordinate system with respect to coupon geometry (Fig. 6a). An example of a cross-section image along the z-axis is also shown (Fig. 6b).

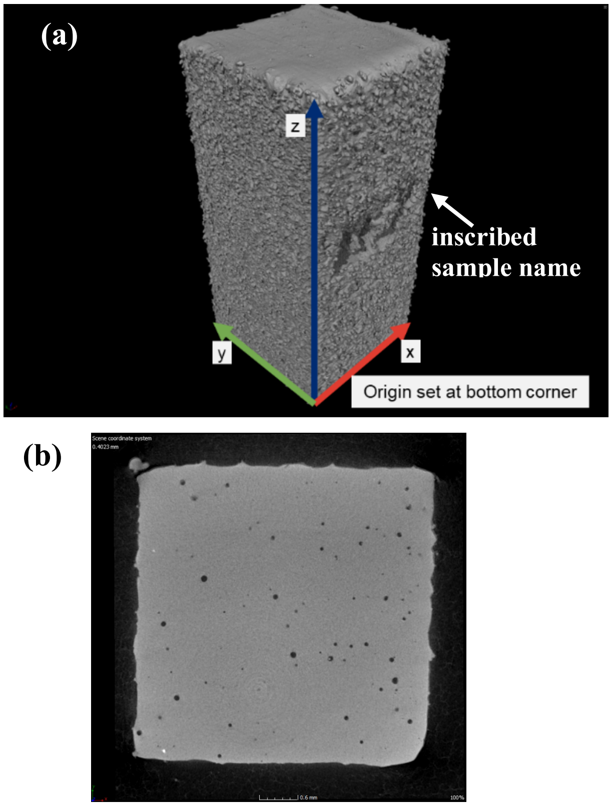

Fig.6 (a) XRCT coordinate system; (b) example of cross-section image across the z-axis.

Automated defect recognition (ADR) was performed using Volume Graphics VGStudio MAX. ADR analysis results in a comprehensive numerical representation of the porosity within the sample. Fig. 7 shows representative XRCT results with an overlay of the ADR results onto the 3D and cross-section images.. The porosity is seen in color in both the 3D and cross section images. The color scale is determined by the pore volume (smaller volumes are blue and larger volumes are red). Additionally, each individual defect or pore can be analyzed with respect to its location and size. The results will be correlated with corresponding IR thermal images to establish the relationship of "process signal – defects" which will be discussed in the next section. Also, XRCT provides cumulative porosity results for each sample as shown in Fig. 8. The average porosity aligns with observation in Fig. 5. The vendor's default parameter (#3) results in the least porosity. In lack-of-fusion conditions (#A and #B), porosity level increases with decrease of laser energy density, and significant porosity volume occurs at nominal laser energy (25% of optimal process condition). When nominal energy is above 100% (#D and #E), porosity increases with increased laser energy.

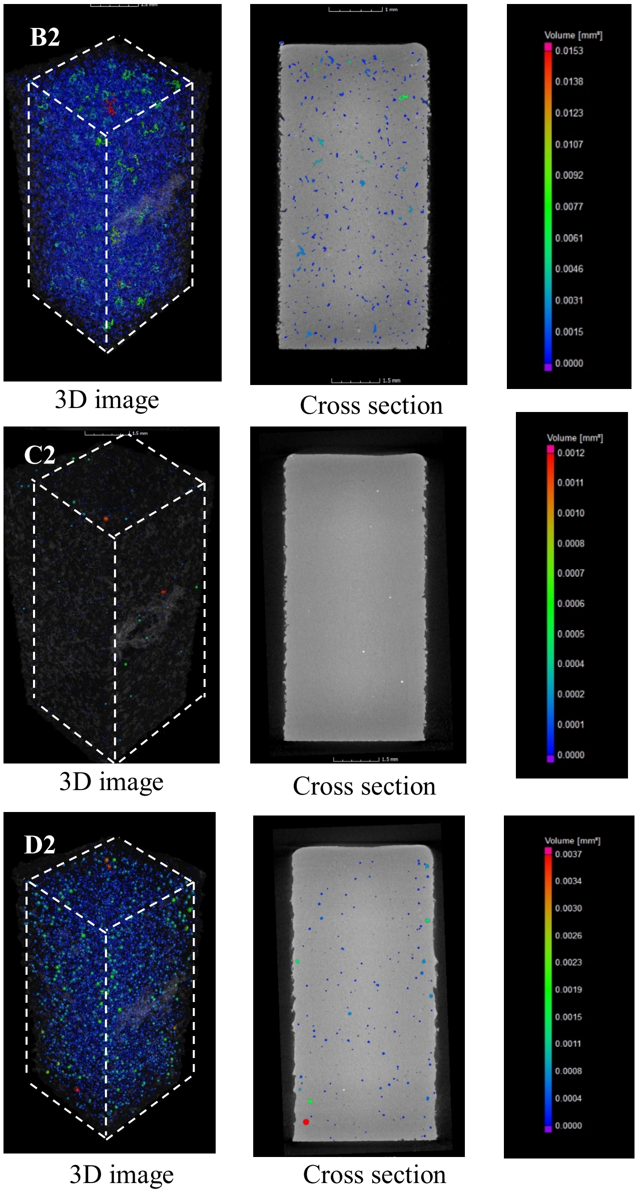

3D image
Cross section

3D image
Cross section

3D image
Cross section

Fig. 7 Representative XRCT results showing porosity of different coupons. Colored pixel indicates pore location and size, white dash line represents boundary of sample.

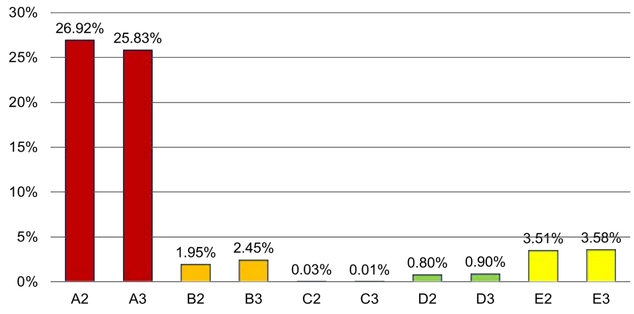

Fig.8 Cumulative porosity volume for different AM samples (5 AM conditions, 2 repeats).

DATA ANALYSIS TO CORRELATE SENSING SIGNALS WITH PROCESS-INDUCED DEFECTS

The entire AM build includes 336 layers with over 6 million images recorded. A total of 30 images from the 10th layer to 300th layer at increments of 10 layers were analyzed in detail. At each layer, the image at the time just before the deposition of powder for the following layer was exported. Similarly, XRCT data was exported into ASCII format as well. It recorded every suspected void and its size, location, and geometry. Then, those results were interpreted using two methods: 1) a statistical analysis to correlate the overall porosity level with sensing signal, and 2) individual void analysis to evaluate the relationship between abnormal signal and pore formation.

Statistical analysis

Fig. 9 shows the sensing signal along the distance in white label at different building times. For each curve, the peak region represents signals reflected from the un-melted powder region between each coupon, and valley region represents sintered coupons. It is found at each curve, each peak value is similar with another, while the valley value varies across different coupons. There is a general trend that coupons made by lower laser density (e.g. #A) lead to a higher valley value.

Additionally, processed signals of each sample were averaged at each layer. Fig. 10 shows the signal value that is averaged across each layer. The signal gets stronger when more and more layers are built. As seen in the figure, there are clear differences among those samples which were built at different energy levels.

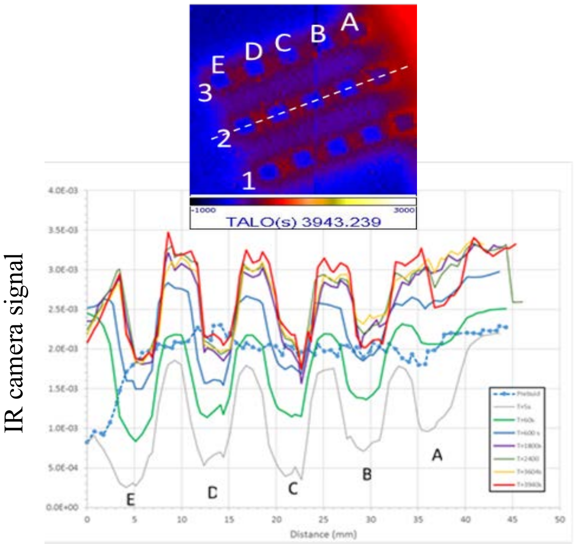

Fig. 9 Radiance *vs.* distance profile at different times.

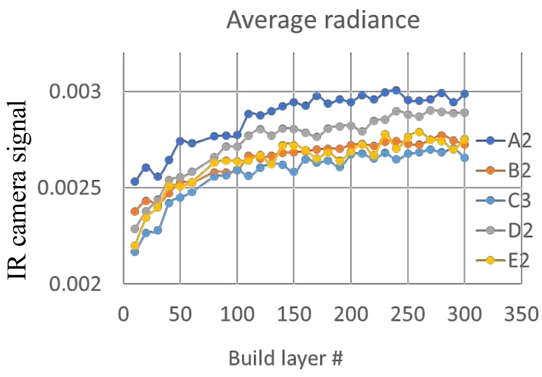

Fig. 10 Averaged monitoring signal at specific layers.

Individual void analysis

Individual void analysis was also performed. It started by analyzing the XRCT results by sorting the suspected voids from largest diameter to smallest diameter. The top 5 largest voids in each sample are used for analysis. So, a total of 50 voids have been analyzed. For each void, its coordinate was extracted first, and then mapped into the coordinate system of the thermal image. It is noted here that each sample orientation in the build plate has been recorded during the AM build process, so it is feasible to map the defect coordinates in the thermal image. The criterion of "detecting" a defect is based on abnormal signal variation at the void location**.** If the sensing signal at the void location is abnormal and exceeds a critical value, it was considered a "hit", which confirmed that sensing signal can reflect the defect. Otherwise, it was considered a "miss". Fig. 11 showed a typical "hit", which is represented by red dot. A void defect in sample D2 was selected, and its coordinates were identified in the XRCT results. Based on the defect's Z coordinate, a relevant image frame will be selected for future analysis. Further, based on a defect's X and Y coordinates, a line that crosses the defect's location will be determined, and the corresponding sensing signal can be plotted. Using this criterion, initially 11 out of 50 voids have been identified in the thermal image, while most voids were not detected. This is due to several reasons: 1) samples A and samples E were built via unrealistic AM conditions, and they have too many voids across the entire samples which are very difficult to detect using current detecting framework; 2) coupons were tilted in the thermal camera, which causes some misalignment between sample defects and image pixel; 3) some voids were located near the sample edge and powder bed, so significant error occurred; and 4) current image pixel size is around 0.76 mm, which is relatively large compare to the void size.

Therefore, in the second analysis, voids from unrealistic AM conditions (samples A & E) were excluded, and effects of sample tilting, image artifact (samples C2 & B3 after 1200 s), and edge effect were considered. The hit rate of the void was approximately 76% (22 voids out of total 29 valid voids). It should be noted that the monitoring accuracy can be further increased by improving the resolution of thermal camera.

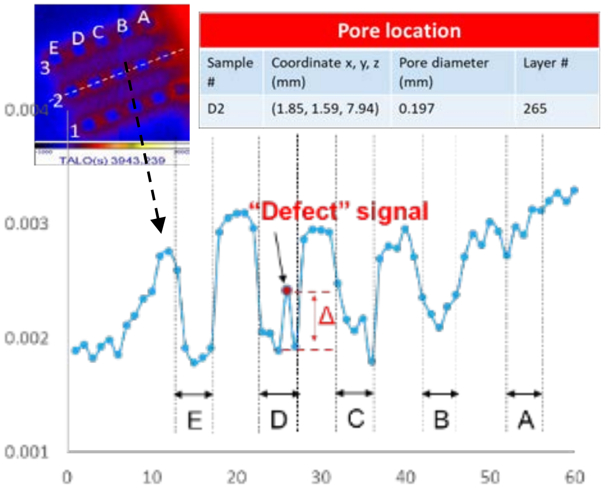
Pore location

Sample #	Coordinate x, y, z (mm)	Pore diameter (mm)	Layer #
D2	(1.85, 1.59, 7.94)	0.197	265

Fig. 11 Detection of individual pore using sensing signal.

ADVANCED AM PROCESS MODELING AND VALIDATION

A series of computational modeling were performed using Sentient's DigitalClone® technique. Sentient's DigitalClone® is a physics-based computational modeling and design framework that simulates the microstructure of different components and their behavior, calculates internal stresses caused by different applied loading conditions, accumulated internal damage resulting in crack nucleation and propagation, and investigates the performance and life prediction. In the past few years, Sentient's DigitalClone® has been enhanced to include an ICME (integrated computational materials engineering) modeling framework for part qualification in metal additive manufacturing (AM). This physics-based multiscale model can be used to qualify material and process parameters and requires minimal calibration. Specifically, the DigitalClone® model can take key AM process parameters (e.g. laser power, scan speed, hatch strategy, layer thickness) as inputs, and simulate part-level distortion and residual stress, as well as the microstructure (e.g. grain structure, porosity) of as-build parts, and fatigue performance when the part is used in the field. In this study, Sentient's DigitalClone® technique is used to optimize defect-repair parameters. For any specific defect, repair parameters need to be customized in order to sufficiently correct existing defects while avoiding the formation of new ones. Different types of simulation were performed for a comprehensive analysis. Those simulations include: 1) melt pool dimension modeling; 2) microstructure and porosity modeling; and 3) defect repair modeling

Melt pool dimension modeling

3-dimensional (3D) heat transfer finite element analysis (FEA) was used to simulate the melt pool dimension. In the analysis, a physics-based heat source model was used that considers major AM process parameters, including laser power, scan speed, hatch space, layer thickness, etc. This will correlate the process parameter with final melt pool dimension, which eventually guides the defect repair action.

In addition to the physics-based heat source model, a solution-dependent-variable (SDV) material model was also used to dynamically update material's properties due to materials state transition (powder-liquid-solid) in AM building process. Material properties significantly change when AM powder transitions to liquid / solid state during the printing process, and the property change will significantly affect simulation accuracy. Sentient's SDV material model can dynamically adapt material properties to different material states, and this ensures the simulation accuracy. Both heat source model and material model were implemented in the commercial FEA package ABAQUS to conduct the heat transfer analysis. Table 2 shows the physical property of AlSi10Mg used in this simulation. Fig. 12 shows the finite element model to simulate the temperature and materials state transition. Powder layer was first melted due to laser heating, and then solidified in the rapid cooling stage when the laser moved away. The temperature history of each node can be obtained.

Table 2. AlSi10Mg properties used in the simulation.

Material state	Density (kg/m^3)	Thermal conductivity (W/m*K)	Specific heat (J/kg·K)
[a] Powder	1350	0.5	915
Solid	2680	110	915

[a] Powder property is estimated.

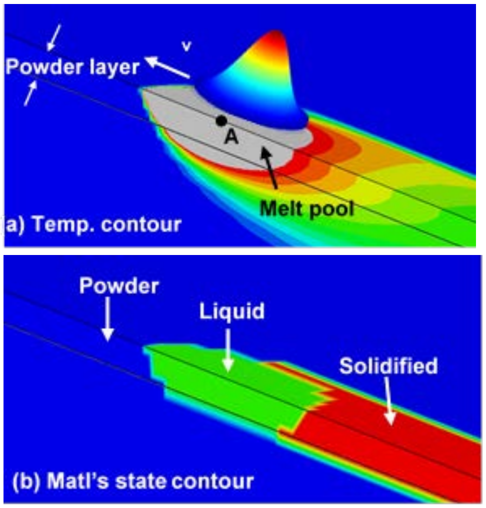

Fig. 12 Finite element model to simulate the temperature and material state transition (power-liquid-solid).

Using the above thermal model, a set of single-track cases with different process parameters has been simulated. It intends to investigate the effect of process parameters on the melt pool size and geometry. A comprehensive understanding of melt pool geometry and size will allow good judgement for defect repair conditions. Table 3 lists the process parameters at different simulation condition.

Table 3. Process conditions for single-track simulation.

Case #	Laser power (W)	Scan speed (mm/s)	Layer thickness (µm)
1	125	1400	30
2	150	1400	30
3	200	1400	30
4	250	1400	30
5	300	1400	30
6	200	700	30
7	200	1000	30
8	200	1800	30
9	200	2000	30

Fig. 13 shows the resulting melt pool geometry at different conditions. As the laser power increases, the melt pools became larger and there size increases in all three dimensions (length, width, and depth). When increasing the laser scan speed, the melt pool tends to become shallower but longer. Fig. 14 shows quantitative analysis, indicating that the melt pool length is most sensitive to process parameters and the melt pool width is the least sensitive. The various melt pool sizes and geometries at different conditions should not be neglected when performing defect repair.

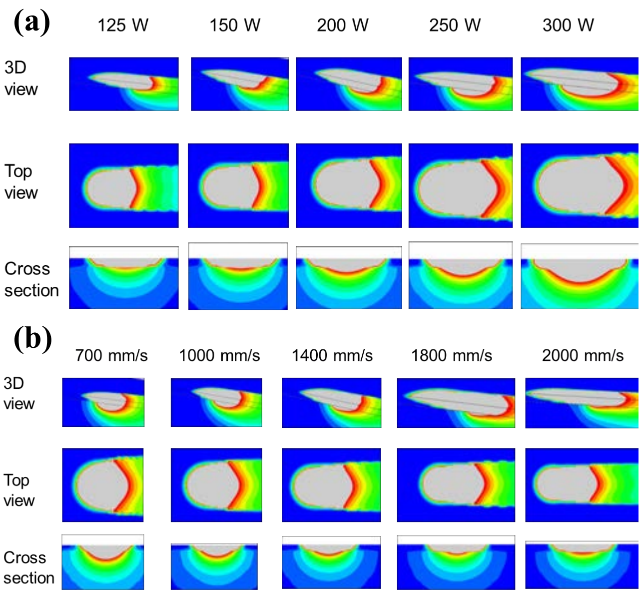

Fig. 13 (a) effect of laser power on melt pool geometry; (b) effect of laser scan speed on melt pool geometry.

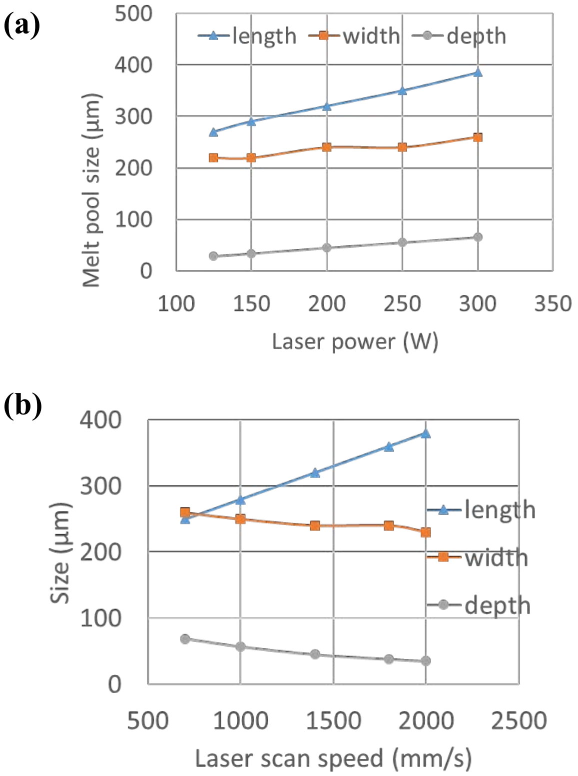

Fig. 14 Quantitative analysis of melt pool size at different laser power and scan speed.

Microstructure and porosity modeling

In addition to single-track simulation, multi-layer and multi-scan simulation was performed to simulate the microstructure and porosity. Actual process conditions listed in Table 1 were used in the simulation. This simulation was done by two steps: 1) thermal modeling in ABAQUS to simulate temperature history; and 2) microstructure modeling in Sentient's in-house code to simulate porosity and grain structure.

In thermal modeling, a total of 20 scans were simulated at each condition (4 layers, 5 scans / layer). Fig. 15 shows the representative peak temperature contour from parameters #C in Table 1. The color represents the peak temperature of each location during the printing process. The other four conditions (#A, #B, #D, #E) show a similar contour but have different magnitudes. The peak temperature increases when increasing laser density from #A to #E.

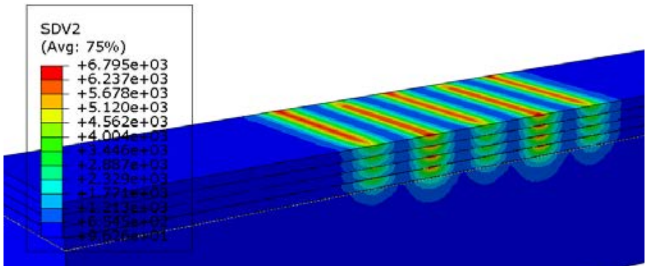

Fig. 15 Representative 3D contour of peak temperature.

Fig. 16 shows the selected 2D cross section of 3D model. The gray area represents the melted and re-solidified region. Simulation results clearly showed the lack of fusion in samples #A and #B, which aligned well with optical microscopic results. Other samples are fully melted, and therefore, it didn't show lack-of-fusion voids in those simulations. It is noted that the porosity due to excessive energy density (samples #D and #E) cannot be captured by commercial FEA software. That porosity will be considered in Sentient's in-code microstructure model.

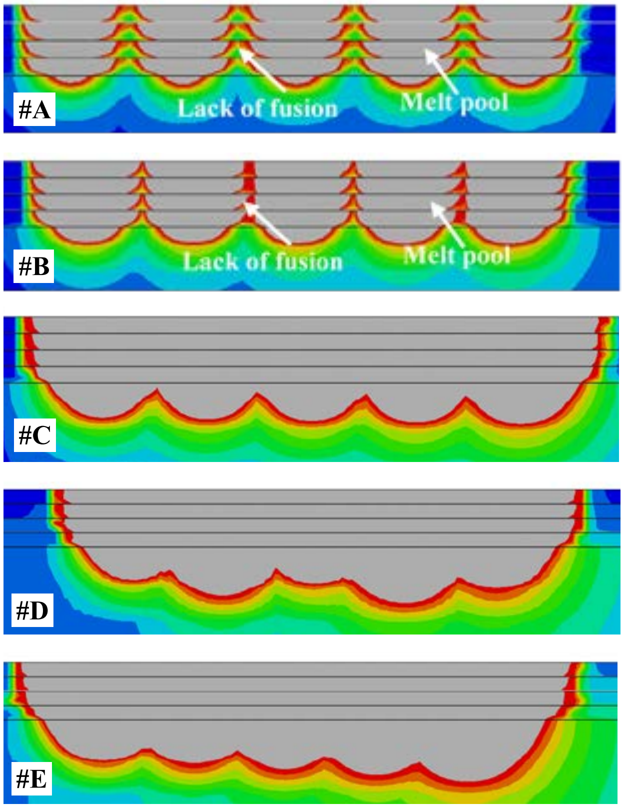

Fig. 16 Cross section of 3D thermal modeling. (gray color represents melted and re-solidified area).

Sentient's microstructure model is a physics-based model that predicts the grain size and morphology. The microstructure model was coupled with thermal modeling, and it is capable of predicting microstructure evolution in additive manufacturing. Fig. 17 shows a general procedure of modeling the microstructure. Thermal modeling is first performed using 3D finite element analysis to calculate the temperature evolution within AM build process. Then, the temperature history in the cross-section of the FEA domain will be projected to a 2D microstructure domain with refined grid size. Finally, melting and solidification behavior will be simulated in the microstructure model.

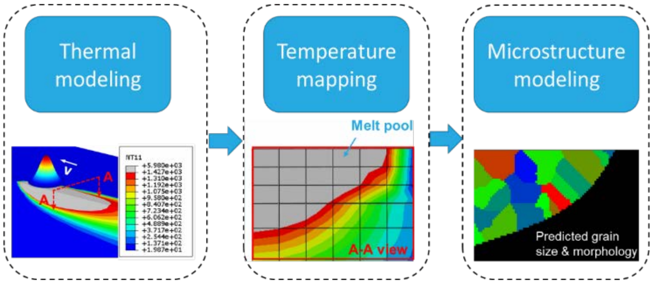

Fig. 17 General procedures to simulate microstructure using Sentient's physics-based model.

After importing the simulated temperature history from thermal modeling, the grain structure and relevant porosity were predicted in the microstructure model for all five conditions. Fig. 18 shows the simulated microstructure results. Color represents grain orientation which ranges from 0° to 90 °. The black area represents voids. As seen from the figure, predicted grain structures mostly show columnar grains, which agrees well with experimental findings [7]. Also, both lack-of-fusion porosity and keyhole / boiling porosity were predicted. The prediction of porosity agrees with experimental results in two aspects: 1) at energy density levels below optimal value, porosity decreases with increase of energy density; while at energy density levels above the optimal value, it increases with an increase of energy density; and 2) voids appear more spherical at high energy density samples (#D and #E) than the low energy density samples (#A and #B).

Fig. 19 compared the predicted porosity levels to experimental results. For the predicted porosity level there is good agreement with experimental results in most cases, except for sample #B which over-predicted the porosity. This is possibly because condition #B is near the transition zone from lack of fusion to fully melt, and the current thermal model is not developed well enough to capture such transition. This thermal model can be improved by calibrating the model coefficients through building more coupon samples.

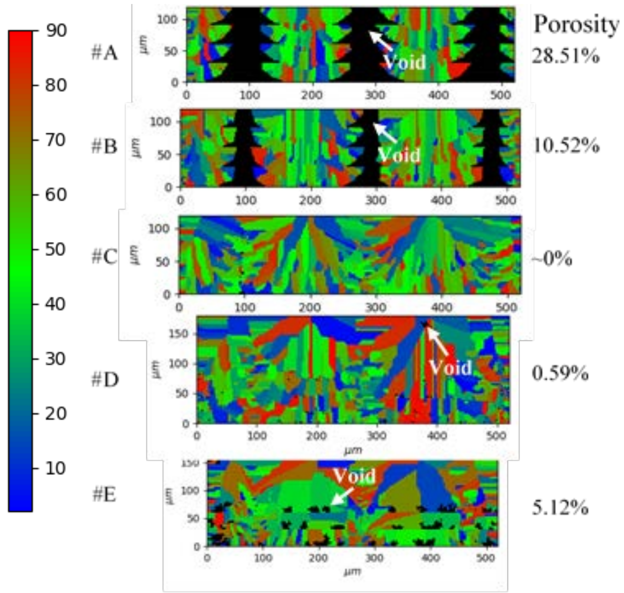

Fig. 18 Simulated microstructure of 5 AM conditions used in this study.

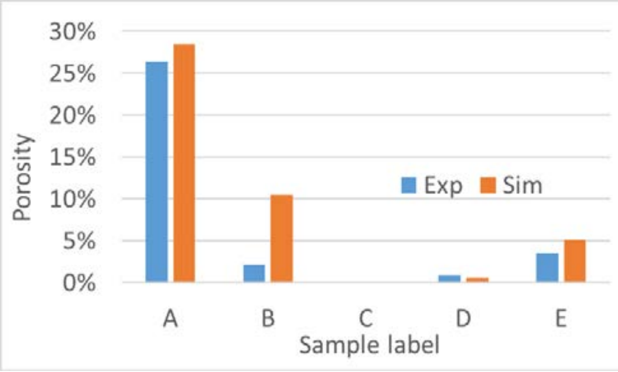

Fig. 19 Comparison of simulation and experiment regarding porosity of 5 conditions.

Defect repair modeling

After validating the microstructure model, repairing artificial defects via laser re-melting technique were computationally tested using different parameters. Firstly, an initial printing process was simulated. Certain process parameters were intentionally selected to generate lack-of-fusion porosity as shown in Fig. 20. As seen in the image, lack-of-fusion voids occur between two neighboring melt pools. Then, defect repair via laser re-melting was simulated after printing each layer and before adding a new powder layer. During the laser re-melting process, the layer hatch was offset from the initial hatch in order to target the void region as shown in Fig. 21. Table 4 lists the original build parameters, and 3 different repair parameters. In the defect repair parameters, repair #1 uses the same parameters as the original build, but with the offsetting hatch as shown in Fig. 21. Repair #2 and repair #3 increases the laser power to 200 W and 250W, respectively.

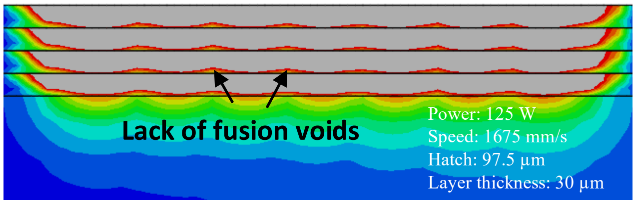

Fig. 20 Simulation of initial build with artificial lack-of-fusion porosity.

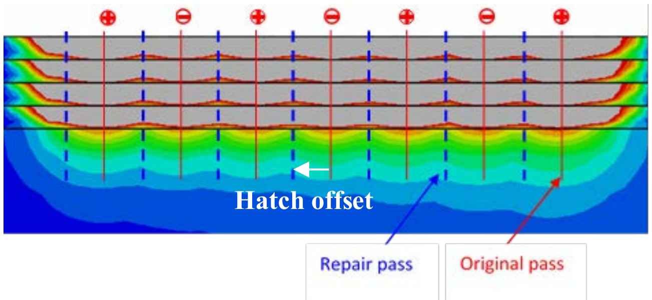

Fig. 21 Schematic of hatch spacing in defect repair via laser re-melting.

Table 4. Process parameters for defect repair.

Case #	Laser power (W)	Scan speed (mm/s)	Layer thickness (μm)
0 (original build)	125	1675	30
1	125	1675	30
2	200	1675	30
3	250	1675	30

Fig. 22 shows 3D modeling results from the original build (4 layers) and repairs (2 layers) using three conditions. As seen from simulation results, repair case 1 used the same build parameters, and there were very limited effects to fix the void. Once increasing the laser power to 200 W, as in case 2, about 50% of the pores have been fixed via laser re-melting. Once further increasing laser power to 250 W, as shown in case 3, all of the pores are repaired, showing a fully dense part. This set of simulation indicates that appropriate laser repair parameters need to be determined to fix the *in-situ* defects.

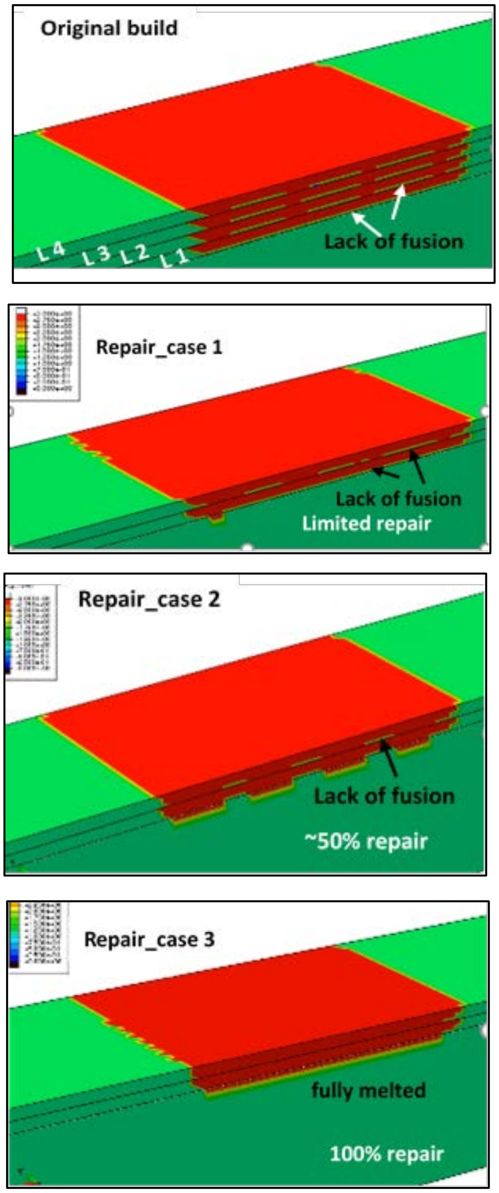

Fig. 22 Defect repair modeling via laser re-melting using different parameters

CONSTRUCTING PROCESS WINDOW FOR OPTIMAL DEFECT-REPAIR PARAMETERS

As discussed above, appropriate laser repair parameters are required to fix the *in-situ* defects without causing additional defects. Therefore, a process window needs to be created prior to the actual AM build, so the optimal laser repair parameters can be immediately determined based on size and geometry of any void. Additional simulation was performed to obtain a comprehensive study of parametric effects on melt pool size and porosity. Laser power and laser scan speed will be used as adjustable parameters for real-time laser repair purpose in this study, because they are two of the adjustable parameters that need minimal control and configuration. Other AM parameters (e.g. powder layer thickness, spot size) will be fixed. Based on experimental coupon samples under 5 conditions (Table 1), additional laser parameters in simulation were limited to the set that has nominal energy density between sample B (50%) and sample D (150%). Any other nominal energy density beyond this limitation has proven to result in high porosity as shown in samples A and E. Therefore, 36 additional simulation conditions have been designed as shown in Table 5.

Table5. Simulation conditions for constructing optimal process window.

Case #	Laser power (W)	Scan speed (mm / s)	Nominal energy density
P1S1	P1	S1	51%
P1S2	P1	S2	57%
P1S3	P1	S3	65%
P1S4	P1	S4	70%
P1S5	P1	S5	76%
P1S6	P1	S6	83%
P2S1	P1	S1	64%
P2S2	P1	S2	72%
P2S3	P1	S3	83%
P2S4	P1	S4	89%
P2S5	P1	S5	97%
P2S6	P1	S6	105%
P3S1	P1	S1	72%
P3S2	P1	S2	81%
P3S3	P1	S3	93%
P3S4	P1	S4	100%
P3S5	P1	S5	108%
P3S6	P1	S6	118%
P4S1	P1	S1	80%
P4S2	P1	S2	90%
P4S3	P1	S3	103%
P4S4	P1	S4	111%
P4S5	P1	S5	120%
P4S6	P1	S6	131%
P5S1	P1	S1	86%
P5S2	P1	S2	97%
P5S3	P1	S3	110%
P5S4	P1	S4	119%
P5S5	P1	S5	129%
P5S6	P1	S6	141%
P6S1	P1	S1	94%
P6S2	P1	S2	105%
P6S3	P1	S3	120%
P6S4	P1	S4	130%
P6S5	P1	S5	141%
P6S6	P1	S6	153%

[a] Laser power increases from P1 to P6, and scan speed decreases from S1 to S6. Actual values are not shown due to intellectual property reasons.

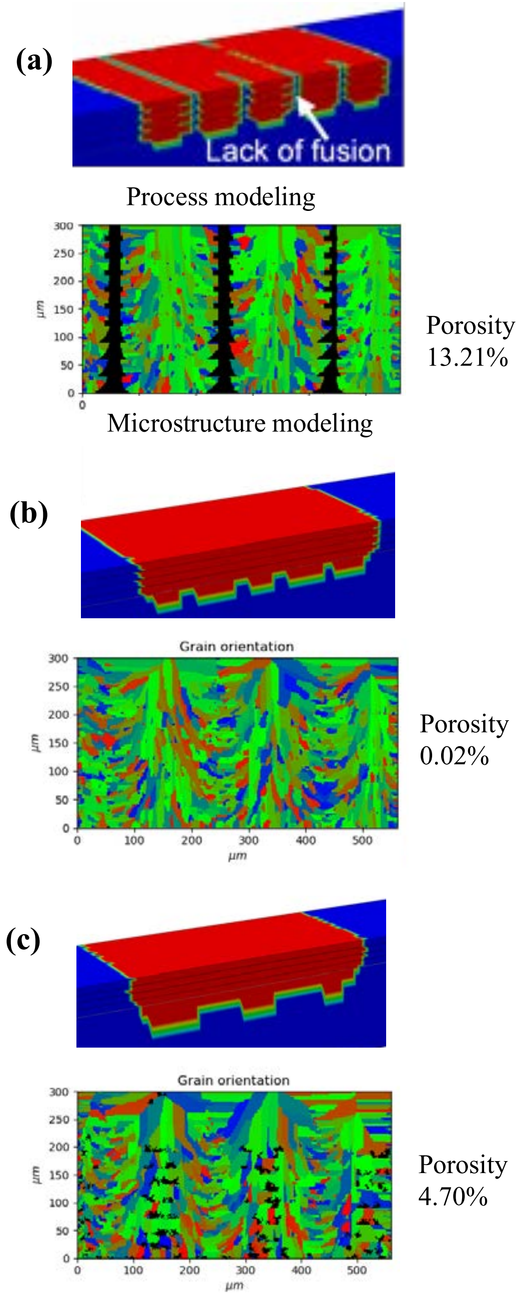

Fig. 23 Representative simulation results at (a) low laser energy density (P1S1); (b) moderate laser energy density (P3S4); (c) high laser energy density (P5S5).

A total of 36 conditions have been simulated in Sentient's process model and microstructure model. In each simulation, the melt pool size and porosity were analyzed. Fig. 23. shows the representative results at 3 conditions (lower energy density, moderate energy density, and high energy density). Simulation results clearly show different temperature and porosity results at different laser powers and speeds. By incorporating the results from all 36 conditions, process windows for printing AlSi10Mg were plotted as shown in Fig. 24. In each figure, the x-axis represents laser power, and the y-axis represents laser scan speed. The contour represents the intensity of objects (e.g. melt pool width, melt pool depth, and porosity). These process windows provide a clear guideline to choose appropriate parameters to repair the voids in real time.

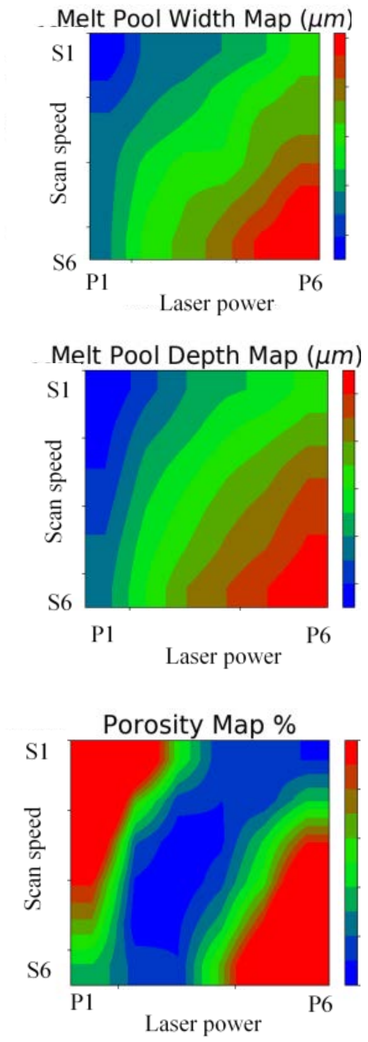

Fig. 24 Process windows in powder bed fusion of AlSi10Mg alloy. (note: physical values are not presented due to intellectual property.)

FOLLOW-ON WORK

The work described above has successfully demonstrated the technical feasibility of *in-situ* monitoring the pore formation in an aluminum alloy during a powder bed fusion process. It also showed that appropriate process parameters are required to correct any defect. The follow-on work is to fully integrate the *in-situ* defect monitoring and correcting technique to develop a prototype AM machine that has a closed-loop feedback system which can automatically detects and repairs defects during printing. To successfully achieve this goal, the technical barrier of acquiring and processing enormous amounts of sensing data in real time needs to be addressed. There is also a need to solve the problem of dynamically determining optimal repair parameters in real time and feeding commands to the machine control system. Sentient is currently working with research institutes, an AM machine vendor, as well as industrial original equipment manufacturer (OEM) to address those technical barriers and integrate those techniques to build a prototype AM machine with close-loop feedback control capability.

CONCLUSIONS

This study demonstrates the technical feasibility of the *in-situ* monitoring of defects and optimizing process parameters via advanced simulation. Key results are listed below:

1) Sensing signal captured by a high-frequency IR camera correlates with porosity defects well in powder bed fusion process of aluminum alloy. Such sensing signals can be used as an indicator to identify process-induced defects in a powder bed fusion process.
2) Porosity defects are affected by laser energy density, with low energy density resulting in lack-of-fusion voids that have irregular shape, while high laser energy density leads to keyhole / boiling voids which tend to be spherical shape.
3) Sentient's multiscale physics-based modeling technique considers the effect of process parameters (e.g. laser power and scan speed) on melt pool geometry, microstructure, and porosity. A process window can be generated using advanced simulation to optimize the process parameters.
4) The current capability of defect monitoring and advanced simulation are presented. A technical path has been identified to demonstrate the feasibility of a closed-loop feedback AM machine to *in-situ* monitor and correct defects for an aluminum alloy component in a powder bed fusion process. Follow-on work is described to successfully achieve this goal.

Author contact: Behrooz Jalalahmadi
bjalalahmadi@sentientscience.com

ACKNOWLEDGMENTS

This work was supported by U.S. Army Combat Capabilities Development Command (CCDC) Award No. W911W6-18-C-0006. Authors would like to express their appreciation to CCDC for its support. Authors also sincerely appreciate technical supports from team members at The Johns Hopkins University Applied Physics Laboratory including Jacob Alldredge, Steven Storck and Sam Kim.

REFERENCES

1. Collins, P. C., Brice, D. A., Samimi, P., Ghamarian, I., and Fraser, H. L., “Microstructural Control of Additively Manufactured Metallic Materials,” *Annual Review of Materials Research*, Vol. 46, 2016, pp. 63–91. DOI: 10.1146/annurev-matsci-070115-031816
2. Mani, M., Feng, S., Lane, B., Donmez, A., Moylan, S., and Fesperman, R., “Measurement science needs for real-time control of additive manufacturing powder bed fusion processes,” NIST Interagency/Internal Report (NISTIR) - 8036, 2015. DOI: 10.6028/NIST.IR.8036
3. Everton, S. K., Hirsch, M., Stravroulakis, P., Leach, R. K., and Clare, A. T., “Review of in-situ process monitoring and in-situ metrology for metal additive manufacturing,” *Materials & Design*, Vol. 95, 2016, pp. 431-445. DOI: 10.1016/j.matdes.2016.01.099
4. Spears, Thomas G., and Scott A. Gold, "In-process sensing in selective laser melting (SLM) additive manufacturing," *Integrating Materials and Manufacturing Innovation* 5:2, 2016. DOI: 10.1186/s40192-016-0045-4
5. Alldredge, J., Slotwinski, J., Storck, S., Kim, S., Goldberg, A., and Montalbano, T., "In-Situ monitoring and modeling of metal additive manufacturing powder bed fusion,” AIP Conference Proceedings, Vol. 1949, (1), April 2018, p. 020007. DOI: 10.1063/1.5031504
6. Yuan, B., Guss, G. M., Wilson, A. C., Hau-Riege, S. P., DePond, P. J., McMains, S., and Giera, B., (2018). “Machine-Learning-Based Monitoring of Laser Powder Bed Fusion”, *Advanced Materials Technologies*, Vol. 3, (12), 2018,1800136. DOI: 10.1002/admt.201800136
7. Thijs, L., Kempen, K., Kruth, J. P., and Van Humbeeck, J, (2013). “Fine-structured aluminium products with controllable texture by selective laser melting of pre-alloyed AlSi10Mg powder,” *Acta Materialia*, Vol. 61, (5), 2013, pp. 1809-1819. DOI: 10.1016/j.actamat.2012.11.052